Journal of Membrane Science 596 (2020) 117704

Contents lists available at ScienceDirect

Journal of Membrane Science

journal homepage: http://www.elsevier.com/locate/memsci

Influence of support layer resistance on oxygen fluxes through asymmetric membranes based on perovskite-type oxides $SrTi_{1-x}Fe_xO_{3-\delta}$

F. Schulze-Küppers [a], S. Baumann [a], W.A. Meulenberg [a,b], H.J.M. Bouwmeester [a,b,*]

[a] Forschungszentrum Jülich GmbH, Institute of Energy and Climate Research-IEK-1, Leo- Brandt-Str. 1, D-52425, Jülich, Germany
[b] Electrochemistry Research Group, Membrane Science and Technology, Faculty of Science and Technology & MESA+ Institute for Nanotechnology, University of Twente, Enschede, the Netherlands

ARTICLE INFO

Keywords:
Perovskite
$SrTi_{1-x}Fe_xO_{3-\delta}$
Asymmetric membranes
Oxygen transport membrane

ABSTRACT

Asymmetric membranes of mixed ionic-electronic conducting perovskite-type oxides $SrTi_{1-x}Fe_xO_{3-\delta}$ (STF, x = 0.3, 0.5 and 0.7) were prepared by inverse sequential tape-casting. Both porous support (~600 μm) and functional membrane layer (~20 μm) for a given membrane assembly were made from the same composition to ensure thermochemical compatibility between the layers. Oxygen fluxes were assessed in the range 650 -1020 °C, using either (non-pressurized) ambient air or pure oxygen as feed gas at the support side of the asymmetric membrane and argon as sweep gas. Notably, similar oxygen fluxes (~1.2×10^{-6} mol cm^{-2} s^{-1}) are measured through the membranes of different compositions above 950 °C when using ambient air as feed gas. This observation is interpreted to reflect the major role of the support layer resistance in rate-limiting the oxygen fluxes through the STF asymmetric membranes, which conclusion is supported by comparison of the oxygen fluxes with those measured previously through asymmetric membranes of $Ba_{0.5}Sr_{0.5}Co_{0.8}Fe_{0.2}O_{3-\delta}$ (BSCF) and $La_{0.6}Sr_{0.4}Co_{0.2}Fe_{0.8}O_{3-\delta}$ (LSCF). A simple diffusion-convection model is used to account for the observed gas phase polarization in the porous support layers limiting the oxygen fluxes.

1. Introduction

With the prospects of obtaining low-cost oxygen, ceramic mixed ionic-electronic conducting (MIEC) oxygen-permeable membranes have attracted considerable attention during the past decades. The envisioned applications range from pure oxygen production [1-2], integration in membrane reactors [3], e.g., for syngas production [4-5] to their implementation in oxy-fuel power plants for CO_2 capture [6-8]. Numerous materials and types of structures, such as perovskites, K_2NiF_4-type and higher order Ruddlesden-Popper phases, have been investigated [9]. One obvious challenge in the field lies in identifying membrane materials, which combine a high oxygen flux and reliability of operation under actual operating conditions, such as CO_2-containing and reducing environments.

High oxygen fluxes are generally realized at high temperatures (e.g. 800–1000 °C), which are ultimately limited by oxygen bulk diffusion. The so-called ambipolar diffusion of the oxygen ions and electrons, being driven by the gradient in oxygen chemical potential across the membrane, may be described by Wagner's equation [10], which predicts that the oxygen flux is inversely proportional to membrane thickness. Therefore, reducing the membrane thickness is an effective way to improve the oxygen fluxes. Below a minimum thickness of about 100–120 μm, however, a porous support is needed to provide mechanical rigidity to the membrane, in particular for planar membranes. Surface exchange rate limitations at the gas/solid interfaces may occur upon reducing membrane thickness. The oxygen surface exchange reaction involves a series of elementary steps such as adsorption and dissociation of oxygen molecules, diffusion of intermediates surface species (e.g., $O^-_{2,\ ads}$, O^-_{ads}), incorporation of oxygen ions into the lattice and reverse steps, each of which may be rate limiting [10]. A thin porous catalytic layer can be deposited on either side of the membrane to overcome the rate limitations associated with oxygen surface exchange [11-12]. Moreover, gas phase transport in the porous support layer, if present, may limit the oxygen fluxes [13-15]. A schematic illustration of the drop in oxygen chemical potential across an asymmetric MIEC membrane is given in Fig. 1.

Support and membrane layers of asymmetric MIEC membranes are commonly made from the same material to ensure chemical and thermal expansion compatibility between the layers. To date a wide variety of techniques has been exploited to fabricate asymmetric membranes such

* Corresponding author. Forschungszentrum Jülich GmbH, Institute of Energy and Climate Research-IEK-1, Leo- Brandt-Str. 1, D-52425, Jülich, Germany.
E-mail address: h.j.m.bouwmeester@utwente.nl (H.J.M. Bouwmeester).

https://doi.org/10.1016/j.memsci.2019.117704
Received 22 August 2019; Received in revised form 28 October 2019; Accepted 28 November 2019
Available online 2 December 2019

as slip casting, tape casting, phase inversion, dip coating, spin coating and screen printing to mention the most commonly used as reviewed by Lemes-Rachadel et al. [16]. Recently, we have identified the perovskite-type oxide $SrTi_{1-x}Fe_xO_{3-\delta}$ (STF) as a promising candidate membrane material [17]. Functional properties, such as ionic and electronic conductivities, thermo-mechanical [18-19] and reducibility [20], affecting the operational reliability of the STF membranes, can be tailored by varying the compositional parameter x in the series. The compositions with high iron contents are reported to exhibit high ionic and electronic conductivities [17,21-22] and fast oxygen surface exchange kinetics [17,21-24], albeit that chemical stability is found to decrease with increasing iron content [17]. In this work, we describe the fabrication of asymmetric planar STF membranes, using the inverse sequential tape-casting technique developed previously in our laboratory [13-15,[13-15], and present a detailed analysis of the data of oxygen permeation.

2. Experimental

Powders of $SrTi_{1-x}Fe_xO_{3-\delta}$ with x = 0.3, 0.5 and 0.7 (abbreviated as STF30, STF50, and STF70) were prepared by solid-state reaction. To this end high-purity $SrCO_3$, Fe_2O_3 and TiO_2 powders (Sigma-Aldrich) were mixed in stoichiometric proportions, dispersed in ethanol, and ball-milled using yttria-stabilized zirconia (YSZ) balls (ø = 5 mm) on a roller bench for 72 h at 100 rpm. The ethanol was evaporated, and the dry powder sieved (300 μm mesh size) and calcined at 1075 °C for 25 h, using heating and cooling rates of 5 °C min^{-1}. The calcined powder was additionally ball milled for 48 h at 100 rpm to obtain a monomodal particle size distribution with d_{10} ~0.5 μm, d_{50} ~1 μm, and d_{90} ~3 μm as determined by dynamic light scattering (Horiba LA 950V2). The obtained STF powder was subsequently dispersed in an azeotropic mixture of ethanol and methyl ethyl ketone, using Nuosperse® FX9086 (Elementis Specialties, Inc.) as a dispersing agent. To this mixture 8 wt% of polyvinyl butyral (Butvar® PVB B-98, Solutia Inc.) was added as a binder, and 4 wt% of Solusolve® 2075 (Solutia Inc.) and 4 wt% of PEG400® (Merck) as plasticizers. The obtained slurry was used for tape casting of the membrane layer. To a part of this slurry 30 wt% of Remy® FG rice starch (Remy Industries NV, Belgium) with a particle size in the range 2–8 μm was added as pore former to prepare the slurry for tape casting of the porous support layer. Prior to use, both slurries were degassed for 10 min at 0.4 bar. Detailed descriptions on the preparation of similar slurries are given elsewhere [13-15].

The inverse sequential tape casting technique was used for preparation of the membrane assembly [13-15]. First, the membrane layer was cast with a blade gap of 50 μm at a casting velocity of 60 mm min^{-1}. The cast membrane layer was left to dry in stationary air at room temperature for 24 h. The support layer was cast on the membrane layer at the same casting velocity with a blade gap of 1.9 mm. After drying overnight in stationary air at room temperature, discs with a diameter of 20 mm were punched from the green tape. The obtained discs were thermally treated at 300 °C, 400 °C and 800 °C for 1 h at each temperature, and finally at 900 °C for 5 h. During this treatment, a static load of 70 g was applied onto each of the discs. The load was removed, and the discs were subsequently annealed in air for 5 h at either 1330 °C, 1300 °C, or 1240 °C for STF30, STF50, and STF70, respectively. Helium leakage tests showed a gas tightness of the membranes of less than 10^{-5} mbar l s^{-1} cm^{-2}.

The structure and phase purity of STF powders and membranes were checked by X-ray diffraction (XRD). XRD patterns were collected on a Bruker D2 PHASER diffractometer, using Cu Kα radiation (1.54184 Å), at room temperature in the 2θ range 20–90° with a step size of 0.0202° and a counting time of 1 s per step. Elemental analysis of the powders was carried out using inductively coupled plasma - optical emission spectrometry (ICP-OES). The microstructure of the membrane and support layers was investigated by scanning electron microscopy (SEM, FEI Phenom, Zeiss Ultra 55). The porosity of support and membrane layers was estimated from SEM micrographs of polished cross sections of fractured asymmetric membranes. Average porosities were obtained from image analysis of at least 10 SEM micrographs of different areas for a given sample. Image analysis was carried out using the analySIS© software package (Olympus Soft Imaging Solutions GmbH, Germany). The mean pore diameter of each porous support layer was determined by mercury intrusion porosimetry (Fisions Instruments, Pascal 440).

A home-made quartz membrane reactor was used for oxygen permeation experiments [25]. The membrane was sealed into the reactor by means of two gold rings. Sealing was achieved by holding the assembly, under a spring load, at a temperature of 1020 °C for 4 h. Oxygen permeation experiments were carried out in the temperature range 650–1020 °C, exposing the support side of the membrane to the feed side gas stream. Ambient air (250 ml min^{1}) or pure oxygen (200 ml min^{-1}) was used as feed gas, while argon (50–280 ml min^{-1}) was used as sweep gas. The oxygen flux was corrected for air ingress into the effluent by continuously measuring the nitrogen concentration in the permeate stream. The oxygen leakage did not exceed 1% of the total measured oxygen flux. Post mortem SEM micrographs of fractured cross sections of the membranes were taken in order to assess whether microstructural changes had occurred during the permeation measurements.

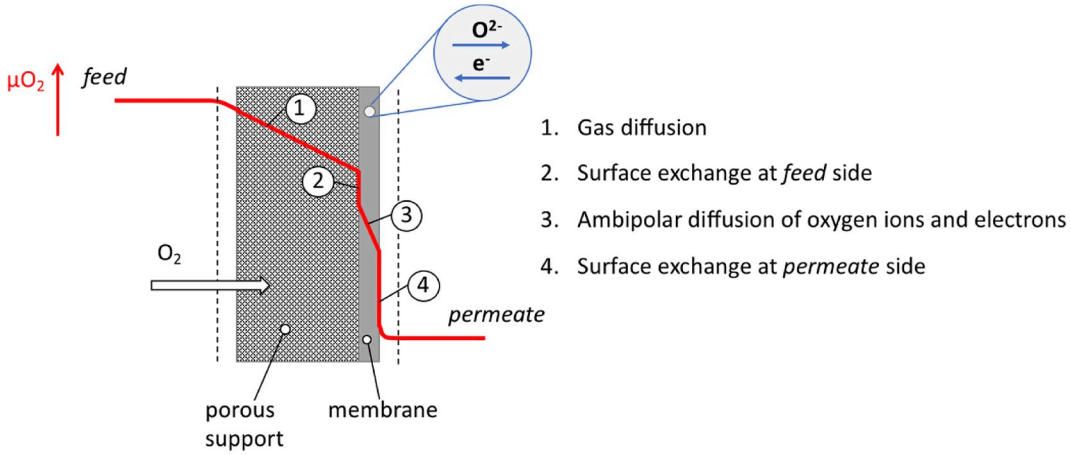

Fig. 1. Schematic illustration of the drop in oxygen chemical potential μ_{O_2} across an asymmetric MIEC membrane during steady-state oxygen permeation.

3. Results and discussion

3.1. Microstructure

SEM micrographs of the cross-sections of fractured asymmetric STF membranes recorded before and after the permeation measurements are shown in Fig. 2. Visual inspection shows no apparent changes in the microstructure of the membranes during the permeation measurements. The results obtained oxygen permeation measurements are discussed in the next section. Relevant parameters related to the microstructure of the membrane layer and porous support determined from the SEM micrographs and from the results of mercury intrusion experiments are compiled in Table 1. As seen from this table, the thickness of the functional membrane layers is in the range 14–24 μm. The porosity in the support layers appears homogeneously distributed and emerges to be the highest for STF30. The latter is attributed to the poor sinter activity of this composition compared to STF50 and STF70. The pore sizes of the support layers are in the range 1.5–2.1 μm. The poorer sinter activity of STF30 is also reflected in a somewhat lower density of the membrane layer for this composition relative to those found for STF50 and STF70. Helium leakage tests, however, confirmed gas tightness in all three cases. No evidence for impurities or second phase formation was found in the XRD patterns of the membranes recorded before and after the oxygen permeation experiments.

3.2. Oxygen permeation

Fig. 3 shows Arrhenius plots of the oxygen fluxes of the asymmetric STF membranes. During measurements either ambient air or pure oxygen was used as feed gas. Also shown in this figure are data from measurements on 1.5-mm-thick disc membranes of different STF compositions, using air as feed gas, from our previous study [17]. It is further important to note that in both studies, the same reactor was employed and the same flow rates of the argon sweep gas (50 ml min^{-1}) were maintained. The curvature of the lines in Fig. 3, *i.e.*, the apparent non-linear Arrhenius behavior, may indicate a change in rate limiting step, but is, at least partly, due to the loss in driving force with increase of temperature. As the sweep gas flow rate was fixed in the experiments, an increase in oxygen flux with increasing temperature reduces the available driving force for oxygen permeation.

The oxygen flux for the disc membranes increases with x in $SrTi_{1-x}Fe_xO_{3-\delta}$, which is accounted for by the concomitant increase in the concentration of oxygen vacancies and, hence, values for the ambipolar conductivity [17]. Due to the reduction in thickness of the functional membrane layer, the asymmetric membranes exhibit higher oxygen permeation fluxes compared to the (unsupported) disc membranes. The increase in oxygen flux is, however, is considerably less than expected on the basis of the inverse relationship between the oxygen flux and membrane thickness predicted by the Wagner equation [10]. Furthermore, the oxygen fluxes of the asymmetric membranes are found to level off at ~1.2×10^{-6} mol cm^{-2} s^{-1} at high temperature if air is used as feed gas. The latter observation is attributed to mass transport losses in the porous support layers, becoming the major factor limiting the oxygen flux at high temperature. The respective support layers impact the oxygen fluxes almost similarly, despite variations found in their porosity and pore diameter (see Table 1). Increasing the sweep gas flow rate from 50 ml min^{-1} to 280 ml min^{-1}, at 900 °C, just below leveling off at the maximum flux, was found to increase the oxygen flux minorly (less than a factor ~1.4). Only after changing the feed gas from air to pure oxygen, thereby eliminating rate limitations by binary gas phase diffusion in the porous support layer, the oxygen fluxes are found to increase substantially, as shown in Fig. 3.

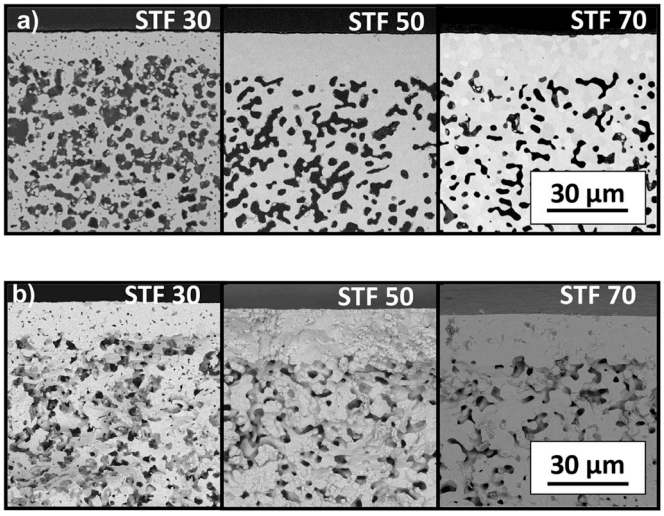

Fig. 2. Cross sectional SEM micrographs of fractured asymmetric STF membranes recorded (a) before (polished) and (b) after oxygen permeation measurements.

Table 1
Microstructural parameters of asymmetric $SrTi_{1-x}Fe_xO_{3-\delta}$ (STF) membranes.

x	Acronym	Membrane layer		Porous support		
		thickness (μm)	porosity (%)	thickness (μm)	porosity (%)	pore diameter (μm)
0.3	STF30	14 ± 1	4.5 ± 1.8	645 ± 20	34.0 ± 0.5	1.6
0.5	STF50	24 ± 1	<1	595 ± 20	26 ± 2	2.1
0.7	STF70	19 ± 2	<1	505 ± 20	23.3 ± 0.9	1.5

3.3. Transport resistance of the porous support layer

The above results make clear that significant mass transport limitations may occur in the porous support layers of the asymmetric STF membranes if air is used as feed gas. Different mechanisms may dominate gas transport in the porous support layer: viscous flow, molecular diffusion and Knudsen diffusion. The relative contribution of ordinary molecular diffusion to Knudsen diffusion to total diffusion can be evaluated via calculation of the Knudsen number K_n, which represents the ratio of the molecular mean free path λ to the pore diameter d_p [26],

$$K_n = \frac{\lambda}{d_p} = \frac{k_B T}{d_p \sqrt{2}\pi\sigma_{ii}^2 P} \quad (1)$$

where σ_{ii} is the collision diameter, k_B is the Boltzmann constant, T is the temperature and P is the pressure. For support pore diameters (see Table 1) and at the temperatures of interest (650–1020 °C), K_n is calculated to be in the range 0.1–0.2, which indicates that gas transport is in the transition flow regime and, hence, all three mechanisms are present. In the calculation, it was assumed that the effective collision diameter can be represented by the mean value of the molecular collision diameters: $\sigma_{O_2-N_2} = (\sigma_{O_2} + \sigma_{N_2})/2$. The molecular collision diameters for oxygen and nitrogen are 3.467 and 3.798 Å, respectively [27].

There is an extensive literature on modelling gas diffusion in porous media using Fick's law, Maxwell-Stefan diffusion equations (MS) or the dusty gas model (DGM). Of these, Fick's law is the simplest and most commonly used for dilute or binary systems. To describe mass transport through the porous support layer, we have adopted the convection-diffusion equation. In this approximation, the total oxygen flux is taken as the sum of the diffusive flux driven by the oxygen concentration difference plus the convective flux of oxygen that is carried along with

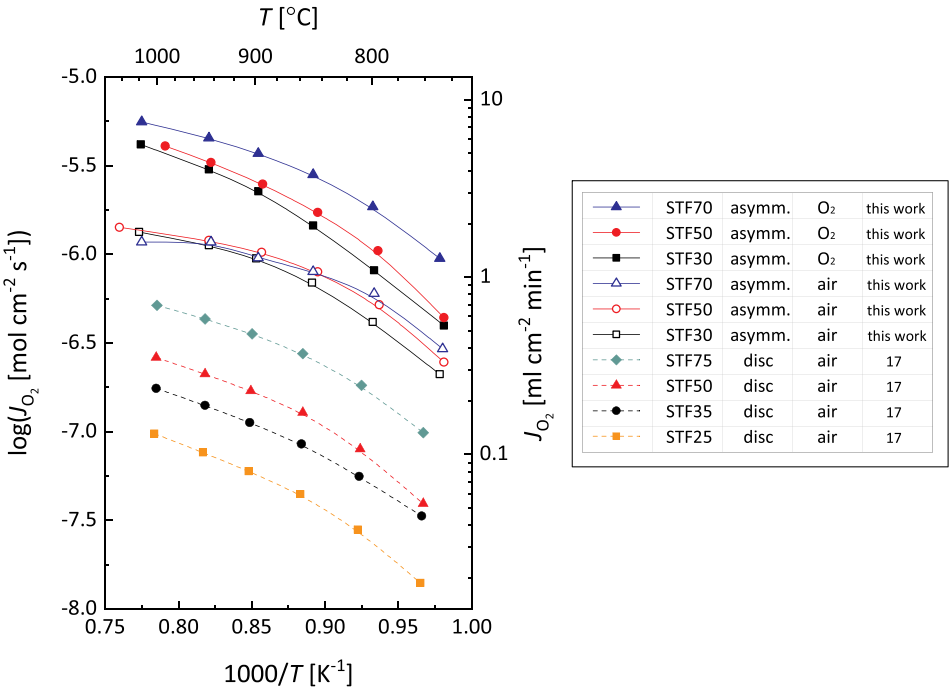

Fig. 3. Temperature dependence of the oxygen permeation fluxes through asymmetric STF membranes. Also shown are oxygen flux data through (unsupported) 1.5 mm-thick disc membranes from our previous work measured under similar conditions [17]. Either ambient air or pure oxygen was used as feed gas (250 ml min^{-1}; see opposite table), while a constant flow (50 ml min^{-1}) of argon was used as sweep gas.

the nitrogen being driven by the absolute pressure difference. The equation for the net oxygen flux through the porous support is derived in the Appendix and can be stated in the form,

$$jO_2 = \frac{D_{O_2}^{eff} P}{RT} \cdot \frac{\left(\ln\left(1 - \frac{pO_{2,\,in}}{P}\right) - \ln\left(1 - \frac{pO_{2,\,ex}}{P}\right)\right)}{L_0} \quad (2)$$

where $pO_{2,in}$ and $pO_{2,ex}$ are the oxygen partial pressures at the pore entry (facing the feed gas) and exit (facing the membrane), respectively, L_0 is the support layer thickness, P is the absolute pressure, R is the gas constant, T is the temperature, and $D_{O_2}^{eff}$ is the effective gas diffusivity, accounting for the effects of the porous medium and gas-solid friction (Knudsen diffusion). Eq. (2) enables calculation of the associated oxygen pressure difference across the porous support layer to sustain a given oxygen flux. Corresponding calculations were performed, assuming that $D_{O_2}^{eff}$ can be represented by [28-29],

$$D_{O_2}^{eff} = \frac{\varepsilon}{\tau^2} \cdot D_0 \quad (3)$$

where D_0 is the gas diffusivity, ε is the porosity, and τ is the tortuosity (actual path length divided by the support layer thickness). D_0 was approximated by using the Bosanquet equation [30],

$$D_0 = \left(\frac{1}{D_{O_2-\,N_2}} + \frac{1}{D_{O_2,Kn}}\right)^{-1} \quad (4)$$

where $D_{O_2-\,N_2}$ ($cm^2\ s^{-1}$) and $D_{O_2,Kn}$ ($cm^2\ s^{-1}$) are the binary gas phase and Knudsen diffusion coefficients, respectively. $D_{O_2-\,N_2}$ was calculated from Fuller's correlation [31].

$$D_{O_2-\,N_2} = \frac{10^{-3} T^{1.75} \left(\frac{1}{M_{O_2}} + \frac{1}{M_{N_2}}\right)}{P\left[(V_{O_2})^{1/3} + (V_{N_2})^{1/3}\right]^2} \quad (5)$$

where M_{O_2} and M_{N_2} are the molar mass (g mol^{-1}) of O_2 and N_2, respectively, and V_{O_2} and V_{N_2} are the corresponding (dimensionless) diffusion volumes. Diffusion volumes for O_2 (16.3) and N_2 (18.5) were taken from a recent compilation of Todd and Young [27]. $D_{O_2,Kn}$ ($cm^2\ s^{-1}$) was calculated from Ref. [32].

$$D_{O_2,Kn} = \frac{d_p}{3} \cdot \sqrt{\frac{8RT}{\pi M_{O_2}}} \quad (6)$$

As Berson et al. [33] reported that the Bruggeman equation is inaccurate for porosities below 40%, we used in this work an expression derived by Kong et al. [34] based on a 3D cube packing,

$$\tau = \frac{(1+\varepsilon)^2}{\varepsilon(1+\varepsilon)^2 + 4\varepsilon^2(1-\varepsilon)} \quad (7)$$

Thus, the calculations show that if non-pressurized ambient air ($pO_{2,in} = 0.21$ atm, $P = 1$ atm) is used as feed gas a large portion of the total available driving force is actually required to sustain the oxygen flux through the porous support layers. Fig. 4 shows the calculated maximum oxygen fluxes that can be sustained though the porous support layers under the given experimental conditions. These fluxes were calculated (using Eq. (1)), assuming that no rate limitations occur due to bulk diffusion and surface exchange and, hence, the total driving force for oxygen transport across the asymmetric membrane is consumed by gas transport through the porous support layer. Under this assumption, the oxygen partial pressure at the pore exit, $pO_{2,ex}$, equals the pO_2 in the sweep gas facing the membrane. Assuming ideal mixing of gases at the permeate side of the membrane, $pO_{2,ex}$ equals the measured pO_2 at the outlet of the reactor. As can be seen from Fig. 4, at the highest temperatures the experimental oxygen fluxes approach the calculated maximum sustainable fluxes through the support layers. Recognizing the limitations of our modelling and the uncertainties in the determination of the parametric input-parameters, such as the diameter of tortuous pores and the effective gas diffusivity [33], we believe that our analysis lends further support to the conclusion that at these high temperatures the support layer resistance exerts a major influence on the oxygen flux through the asymmetric STF membranes.

Fig. 5 shows a comparison of the oxygen fluxes through the

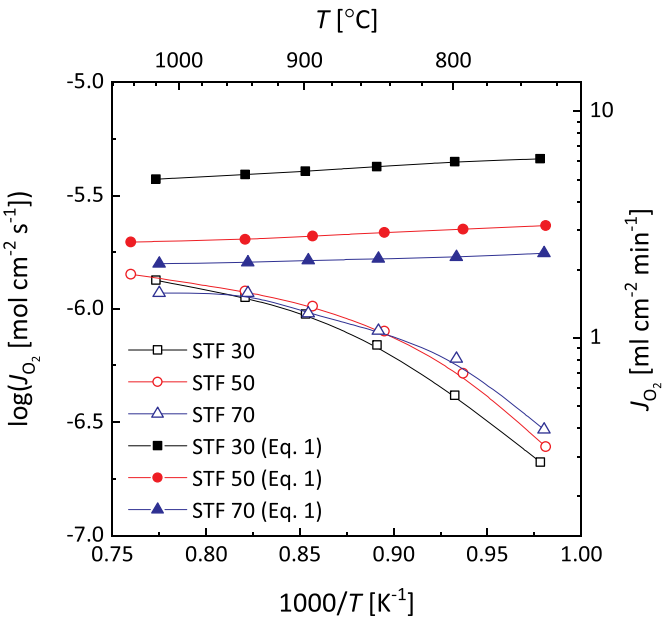

Fig. 4. Comparison of the experimental oxygen fluxes through asymmetric STF membranes measured using ambient air as feed gas (data from Fig. 3) with those calculated using Eq. (1), assuming limiting gas transport across the porous support layers.

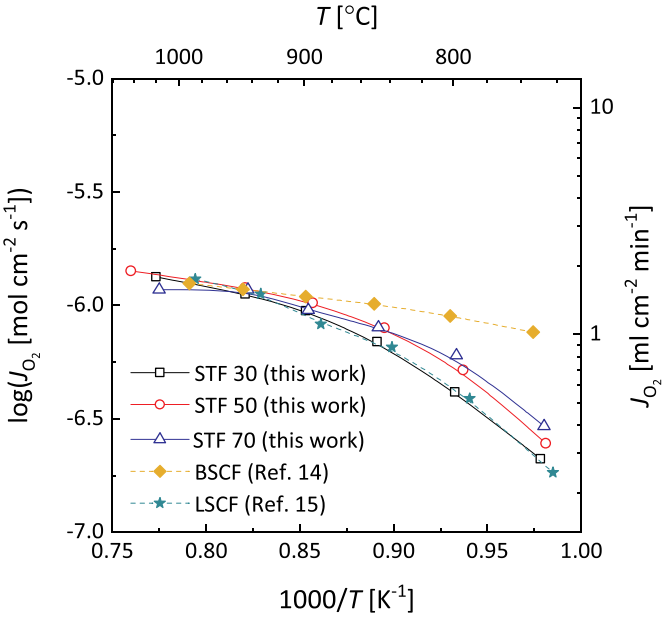

Fig. 5. Comparison of the oxygen fluxes through asymmetric STF membranes (data from Fig. 3) with those measured through asymmetric BSCF [14] and LSCF [15] membranes. In all cases ambient air was used as feed gas (250 ml min^{-1}), while a constant flow (50 ml min^{-1}) of argon was used as sweep gas.

asymmetric STF membranes with those measured through asymmetric membranes of $La_{0.6}Sr_{0.4}Co_{0.2}Fe_{0.8}O_{3-\delta}$ (LSCF) and $Ba_{0.5}Sr_{0.5}Co_{0.8}Fe_{0.2}O_{3-\delta}$ (BSCF) from our previous studies [14,15]. In all cases ambient air was used as the feed gas (250 ml min^{-1}), while a constant flow (50 ml min^{-1}) of argon was used as sweep gas. Despite the different compositions, all membranes are found to exhibit similar oxygen fluxes above ~ 950 °C. This observation is in support of our conclusion that at these high temperatures, gas transport in the porous support layers is the main source of concentration polarization in the asymmetric membranes. The notable agreement between the oxygen fluxes above ~ 950 °C suggests that the porous supports of the asymmetric membranes have very similar microstructures. As for the asymmetric STF membranes in this study, the porous supports of the LSCF and BSCF membranes in our previous study were prepared using rice starch as the pore-forming agent, thereby ensuring similar microstructures. Experiments are underway to verify the conclusions in this study by measuring the oxygen fluxes through asymmetric membranes of the same composition having porous support layers with different porosities and pore sizes prepared by the use of different pore-formers.

4. Summary and conclusions

In summary, it is found that the porous supports, showing apparent porosities and pore diameters in the ranges 23–34% and 1.5–2.1 μm, respectively, exert a major influence on the rate of oxygen permeation through asymmetric all-STF membranes when (non-pressurized) ambient air is used as feed gas. Notably, similar oxygen fluxes (~1.2×10^{-6} mol cm^{-2} s^{-1}) are measured through all three membranes of different compositions investigated in this work above 950 °C. This conclusion is further supported by the results from convection-diffusion model simulations and by comparison of the oxygen fluxes with those measured previously through asymmetric membranes of $Ba_{0.5}Sr_{0.5}Co_{0.8}Fe_{0.2}O_{3-\delta}$ (BSCF) and $La_{0.6}Sr_{0.4}Co_{0.2}Fe_{0.8}O_{3-\delta}$ (LSCF) having similar microstructures of the porous support layers. The obtained results urge for optimization of gas transport through the porous supports (e.g., by reducing tortuosity) and/or adaptation of the operational parameters (e.g., by using a pressurized air feed side) to enhance the oxygen permeation fluxes.

Declaration of competing interest

There are no interests to declare.

Acknowledgements

The authors would like to thank Dr. Y.J. Sohn for crystal structure analysis by X-ray diffraction and Mr. S. Heinz for conducting oxygen permeation measurements.

Appendix A. Derivation of Eq. (1)

The mass balance equation for the molar oxygen flux through the porous support layer at steady state reads

$$j_{O_2} = -D_{O_2}^{eff} \nabla c_{O_2} - c_{O_2} \cdot \left(\frac{B_0}{\mu} \nabla P \right) \quad (A.1)$$

where $D_{O_2}^{eff}$ is the effective diffusion coefficient, c_{O_2} the gas phase oxygen concentration, B_0 the (effective) permeability or viscous flow parameter, μ the viscosity coefficient and P the total pressure. The diffusion coefficient is written as an effective diffusion coefficient to account for the effects of the porous medium and gas-solid friction (Knudsen diffusion). Eq. (A.1) is also often referred to as the advection-diffusion, drift-diffusion or extended diffusion equation.

Oxygen permeating through the supported membrane layer drives both convective and diffusive oxygen fluxes across the support. The total oxygen flux equals the sum of the diffusive flux driven by the oxygen concentration difference plus the convective flux of oxygen that is carried along with the nitrogen driven by the pressure difference, as expressed by Eq. (A.1). Darcy's law

$$v = -\frac{B_0}{\mu}\nabla P \tag{A.2}$$

relates the pressure gradient to the molar average velocity of the gas ν, which for the O_2–N_2 binary mixture reads

$$\nu = \frac{c_{O_2}\nu_{O_2} + c_{N_2}\nu_{N_2}}{c_{tot}} = \frac{j_{O_2} + j_{N_2}}{c_{tot}} \tag{A.3}$$

where $c_{tot} = c_{O_2} + c_{N_2}$ is the total gas concentration, and ν_{O_2} and ν_{N_2} are the molar velocities of oxygen and nitrogen, respectively, and j_{N_2} is the nitrogen flux. At steady state, $j_{N_2} = 0$, since the convective flux of nitrogen is balanced by an equal, but opposite diffusive flux. Substitution of the obtained result in Eq. (A.1) gives

$$j_{O_2} = -D_{O_2}^{eff}\nabla c_{O_2} + \frac{c_{O_2}}{c_{tot}} j_{O_2} \tag{A.4}$$

Noting that only a very small pressure drop is needed to balance the outgoing diffusive nitrogen flux, the total pressure P in the porous support remains virtually constant. By assuming an ideal gas mixture, so that Dalton's law can be used, Eq. (A.4) can be re-shuffled to yield the simple relationship

$$j_{O_2} = \frac{D_{O_2}^{eff} P}{RT}\nabla \ln\left(1 - \frac{pO_2}{P}\right) \tag{A.5}$$

where R is the gas constant. Integrating Eq. (A.5) over the support thickness L yields Eq. (1)

$$j_{O_2} = \frac{D_{O_2}^{eff} P}{RT}\cdot\frac{\left(\ln\left(1 - \frac{pO_{2,\ in}}{P}\right) - \ln\left(1 - \frac{pO_{2,\ ex}}{P}\right)\right)}{L} \tag{1}$$

where $pO_{2,in}$ and $pO_{2,ex}$ are the pO_2's at the entry and exit of the pore, respectively. In derivation of Eq. (1) there is no need to assume that the effective diffusion coefficients for O_2 and N_2 components in the binary gas mixture are similar. In fact, these may be dissimilar on account of differences in gas-solid interactions and molar fluxes due to differences in the molecular weights of both molecules.

Eq. (1) can be used to demonstrate that the diffusive flux is enhanced by convection. The term $\ln(1 - pO_{2,\ ex}/P)$ in Eq. (1) vanishes if $pO_{2,ex} \rightarrow 0$. In this case, the error made by neglecting convection, i.e. assuming a simple diffusive approximation, is 12.2% if air ($pO_{2,in}/P = 0.21$) is used as feed gas. This result confirms that gas phase diffusion is the main source of concentration polarization in porous supports [35], which includes porous electrodes [36]. Eq. (1) predicts that the error increases to 100% if ($pO_{2,in}/P = 0.8$), where the oxygen flux is equally driven by diffusion and convection. Note further from Eq. (1), that the oxygen flux scales linearly with the absolute pressure maintained at the feed side of the porous support layer. A pressurized rather than a non-pressurized ambient air feed may therefore be employed to mitigate the problem of polarization losses in porous support layers.

References

[1] L.L. Anderson, P.A. Armstrong, R.R. Broekhuis, M.F. Carolan, J. Chen, M. D. Hutcheon, et al., Advances in ion transport membrane technology for oxygen and syngas production, Solid State Ion. 288 (2016) 331–337, https://doi.org/10.1016/j.ssi.2015.11.010.

[2] X.-Y. Wu, A.F. Ghoniem, Mixed ionic-electronic conducting (MIEC) membranes for thermochemical reduction of CO2: a review, Prog. Energy Combust. Sci. 74 (2019) 1–30, https://doi.org/10.1016/j.pecs.2019.04.003.

[3] W. Deibert, M.E. Ivanova, S. Baumann, O. Guillon, W.A. Meulenberg, Ion-conducting ceramic membrane reactors for high-temperature applications, J. Membr. Sci. 543 (2017) 79–97, https://doi.org/10.1016/j.memsci.2017.08.016.

[4] A. Arratibel Plazaola, A. Cruellas Labella, Y. Liu, N. Badiola Porras, D.A. Pacheco Tanaka, M. van Sint Annaland, et al., Mixed ionic-electronic conducting membranes (MIEC) for their application in membrane reactors: a review, Processes 7 (2019), https://doi.org/10.3390/pr7030128.

[5] C.F. Miller, J. Chen, M.F. Carolan, E.P. Foster, Advances in ion transport membrane technology for Syngas production, Catal. Today 228 (2014) 152–157, https://doi.org/10.1016/j.cattod.2013.11.012.

[6] M. Puig-Arnavat, M. Sogaard, K. Hjuler, J. Ahrenfeldt, U.B. Henriksen, P. V. Hendriksen, Integration of oxygen membranes for oxygen production in cement plants, Energy 91 (2015) 852–865, https://doi.org/10.1016/j.energy.2015.08.109.

[7] N. Nauels, S. Herzog, M. Modigell, C. Broeckmann, Membrane module for pilot scale oxygen production, J. Membr. Sci. 574 (2019) 252–261, https://doi.org/10.1016/j.memsci.2018.12.061.

[8] F. Schulze-Kuppers, F. Drago, L. Ferravante, S. Herzog, S. Baumann, P. Pinacci, et al., Design and fabrication of large-sized planar oxygen transport membrane components for direct integration in oxy-combustion processes, Separ. Purif. Technol. 220 (2019) 89–101, https://doi.org/10.1016/j.seppur.2019.03.052.

[9] J. Sunarso, S. Baumann, J.M. Serra, W.A. Meulenberg, S. Liu, Y.S. Lin, et al., Mixed ionic-electronic conducting (MIEC) ceramic-based membranes for oxygen separation, J. Membr. Sci. 320 (2008) 13–41, https://doi.org/10.1016/j.memsci.2008.03.074.

[10] H.J.M. Bouwmeester, A.J. Burggraaf, in: P.J. Gellings, H.J.M. Bouwmeester (Eds.), The CRC Handbook of Solid State Electrochemistry, CRC press, Boca Raton, 1996, p. 481, 1997.

[11] H. Kusaba, Y. Shibata, K. Sasaki, Y. Teraoka, Surface effect on oxygen permeation through dense membrane of mixed-conductive LSCF perovskite-type oxide, Solid State Ion. 177 (2006) 2249–2253, https://doi.org/10.1016/j.ssi.2006.05.038.

[12] S. Baumann, P. Niehoff, F. Schulze-Küppers, M. Ramasamy, W.A. Meulenberg, O. Guillon, The role of solid-gas electrochemical interfaces for mixed ionic electronic conducting oxygen transport membranes, in: ECS Transactions, The Electrochemical Society, 2015, pp. 21–33, https://doi.org/10.1149/06602.0021ecst.

[13] S. Baumann, J.M. Serra, M.P. Lobera, S. Escolástico, F. Schulze-Küppers, W. A. Meulenberg, Ultrahigh oxygen permeation flux through supported

Ba0.5Sr0.5Co0.8Fe0.2O3-δ membranes, J. Membr. Sci. 377 (2011) 198–205, https://doi.org/10.1016/j.memsci.2011.04.050.
[14] F. Schulze-Küppers, S. Baumann, W.A. Meulenberg, D. Stöver, H.P. Buchkremer, Manufacturing and performance of advanced supported Ba0.5Sr0.5Co0.8Fe0.2O3−δ (BSCF) oxygen transport membranes, J. Membr. Sci. 433 (2013) 121–125, https://doi.org/10.1016/j.memsci.2013.01.028.
[15] F. Schulze-Küppers, S. Baumann, F. Tietz, H.J.M. Bouwmeester, W.A. Meulenberg, Towards the fabrication of La0.98−xSrxCo0.2Fe0.8O3−δ perovskite-type oxygen transport membranes, J. Eur. Ceram. Soc. 34 (2014) 3741–3748, https://doi.org/10.1016/j.jeurceramsoc.2014.06.012.
[16] P. Lemes-Rachadel, G.S. Garcia, R.A.F. Machado, D. Hotza, J.C.D.D. Costa, Current developments of mixed conducting membranes on porous substrates, Mater. Res. 17 (2009) 242–249, https://doi.org/10.1016/j.ijggc.2008.11.003.
[17] F. Schulze-Küppers, S.F.P. ten Donkelaar, S. Baumann, P. Prigorodov, Y.J. Sohn, H. J.M. Bouwmeester, et al., Structural and functional properties of SrTi1−xFexO3−δ (0≤x≤1) for the use as oxygen transport membrane, Separ. Purif. Technol. (2014), https://doi.org/10.1016/j.seppur.2014.12.020.
[18] R.O. Silva, J. Malzbender, F. Schulze-Kueppers, S. Baumann, O. Guillon, Mechanical properties and lifetime predictions of dense SrTi1-xFexO3-delta (x=0.25, 0.35, 0.5), J. Eur. Ceram. Soc. 37 (2017) 2629–2636, https://doi.org/10.1016/j.jeurceramsoc.2017.02.038.
[19] R.O. Silva, J. Malzbender, F. Schulze-Kueppers, S. Baumann, M. Krueger, O. Guillon, Creep behaviour of dense and porous SrTi0.75Fe0.25O3-delta for oxygen transport membranes and substrates, J. Eur. Ceram. Soc. 38 (2018) 5067–5073, https://doi.org/10.1016/j.jeurceramsoc.2018.07.030.
[20] Y. Liu, V. Motalov, S. Baumann, D. Sergeev, M. Müller, Y.J. Sohn, et al., Thermochemical stability of Fe- and co-functionalized perovskite-type $SrTiO_3$ oxygen transport membrane materials in syngas conditions, J. Eur. Ceram. Soc. (2019), https://doi.org/10.1016/j.jeurceramsoc.2019.06.045.
[21] W. Jung, H.L. Tuller, Impedance study of SrTi1-xFexO3-delta (x=0.05 to 0.80) mixed ionic-electronic conducting model cathode, Solid State Ion. 180 (2009) 843–847, https://doi.org/10.1016/j.ssi.2009.02.008.
[22] S. Molin, W. Lewandowska-Iwaniak, B. Kusz, M. Gazda, P. Jasinski, Structural and electrical properties of Sr(Ti, Fe)O3-delta materials for SOFC cathodes, J. Electroceram. 28 (2012) 80–87, https://doi.org/10.1007/s10832-012-9683-x.
[23] C. Argirusis, F. Jomard, S.F. Wagner, W. Menesklou, E. Ivers-Tiffée, Study of the oxygen incorporation and diffusion in Sr(Ti0.65Fe0.35)O3 ceramics, Solid State Ion. 192 (2011) 9–11, https://doi.org/10.1016/j.ssi.2010.02.016.
[24] C.-Y. Yoo, H.J.M. Bouwmeester, Oxygen surface exchange kinetics of SrTi 1−x Fe x O 3−δ mixed conducting oxides, Phys. Chem. Chem. Phys. 14 (2012) 11759–11765, https://doi.org/10.1039/C2CP41923H.
[25] S. Baumann, F. Schulze-Küppers, S. Roitsch, M. Betz, M. Zwick, E.M. Pfaff, et al., Influence of sintering conditions on microstructure and oxygen permeation of Ba0.5Sr0.5Co0.8Fe0.2O3-δ (BSCF) oxygen transport membranes, J. Membr. Sci. 359 (2010) 102–109, https://doi.org/10.1016/j.memsci.2010.02.002.
[26] R. Krishna, J.A. Wesselingh, The Maxwell-Stefan approach to mass transfer, Chem. Eng. Sci. 52 (1997) 861–911.
[27] B. Todd, J.B. Young, Thermodynamic and transport properties of gases for use in solid oxide fuel cell modelling, J. Power Sources 110 (2002) 186–200, https://doi.org/10.1016/S0378-7753(02)00277-X.
[28] N. Epstein, On tortuosity and the tortuosity factor in flow and diffusion through porous media, Chem. Eng. Sci. 44 (1989) 777–779.
[29] C.L. Tsai, V.H. Schmidt, Tortuosity in anode-supported proton conductive solid oxide fuel cell found from current flow rates and dusty-gas model, J. Power Sources 196 (2011) 692–699.
[30] J.W. Veldsink, R.M.J. van Damme, G.F. Versteeg, W.P.M. van Swaaij, The use of the dusty-gas model for the description of mass transport with chemical reaction in porous media, Chem. Eng. J. Biochem. Eng. J. 57 (1995) 115–125, https://doi.org/10.1016/0923-0467(94)02929-6.
[31] N.E. Fuller, D.P. Schettler, J.E. Giddings, New method for prediction of binary gas-phase diffusion coefficients, Ind. Eng. Chem. 58 (5) (1996) 18–27.
[32] B. Bird, W. Stewart, E. Lightfoot, Transport Phenomena, second ed., Wiley & Sons, New York, 2002.
[33] A. Berson, H.-W. Choi, J.G. Pharoah, Determination of the effective gas diffusivity of a porous composite medium from the three-dimensional reconstruction of its microstructure, Phys. Rev. E - Stat. Nonlinear Soft Matter Phys. 83 (2011), 026310, https://doi.org/10.1103/PhysRevE.83.026310.
[34] W. Kong, Q. Zhang, X. Xu, D. Chen, A simple expression for the tortuosity of gas transport paths in solid oxide fuel cells' porous electrodes, Energies 8 (2015) 13953–13959, https://doi.org/10.3390/en81212406.
[35] X. Chang, C. Zhang, X. Dong, C. Yang, W. Jin, N. Xu, Experimental and modeling study of oxygen permeation modes for asymmetric mixed-conducting membranes, J. Membr. Sci. 322 (2008) 429–435, https://doi.org/10.1016/j.memsci.2008.05.061.
[36] Y. Fu, Y. Jiang, S. Poizeau, A. Dutta, A. Mohanram, J.D. Pietras, et al., Multicomponent gas diffusion in porous electrodes, J. Electrochem. Soc. 162 (2015) F613–F621, https://doi.org/10.1149/2.0911506jes.